

# HST/FOS Spectral Mapping of V2051 Ophiuchi in a Low State

R. K. Saito and R. Baptista

*Departamento de Física, Universidade Federal de Santa Catarina, Brazil*

## ABSTRACT

We report a study of the spectra and structure of the accretion disk of the dwarf nova V2051 Ophiuchi while the star was in an unusual faint brightness state during 1996. The differences between the UV resonant lines and continuum disk surface brightness distributions indicate a vertically extended disk with the emission from these lines arising from the upper atmospheric layers. Distinct emission along the stream trajectory suggests the occurrence of gas stream overflow. Spatially resolved spectra show that the lines are in emission at all disk radii. The Balmer decrement becomes shallower with increasing radius. The FWHMs of the emission lines show differences with respect to that expected for a gas in Keplerian rotation and the line intensities drop with a radial dependency of  $I \propto R^{-1.78}$ . The uneclipsed light contributes about 5 - 10 per cent of the total flux, and its spectrum is dominated by a Balmer jump and strong lines in emission. Broad absorption bands, possibly due to Fe II, are present in the spectra of the disk side farther away from the secondary star, suggesting it arises from absorption by a extended gas region above the disk; the differences between the spectra of the hemisphere farther from and nearer to the secondary star are interpreted in terms of chromospheric emission from a disc with a non-negligible opening angle (limb brightening effect). Stellar atmosphere model fits to the extracted white dwarf spectrum lead to a temperature  $T_{WD} = 9500^{+2900}_{-1900} K$  and a distance of  $d = 67^{+22}_{-25} pc$  if the inner disk is opaque, or  $d = 92^{+30}_{-35} pc$  if the inner disk is optically thin.

*Subject headings:* stars: cataclysmic variables – accretion disks, dwarf novae – individual: V2051 Oph

## 1. Introduction

V2051 Ophiuchi was discovered by Sanduleak (1972). It is a dwarf nova, a compact binary in which mass is fed to a white dwarf (the primary star) by a Roche lobe filling late-type star (the secondary) via an accretion disk. V2051 Oph shows recurrent but sparse outbursts in which the disk expands and brightens by 2-3 magnitudes during 1-3 days ( $B \simeq 13 mag$  at maximum, Bateson 1980; Warner & Cropper 1983; Warner & O'Donoghue 1987) as a consequence of a sudden increase in mass accretion through the disk. In the quiescent, low-mass accretion state, the white dwarf and the bright spot (formed by the impact of the infalling gas stream with the outer edge of the disk) dom-

inate the light from the binary at optical and ultraviolet wavelengths, and the optical spectrum shows double-peaked H I and He II emission lines which exhibit the classical rotational disturbance effect during eclipse (Cook & Brunt 1983; Watts et al. 1986).

The binary is seen at a high inclination angle ( $i = 83^\circ$ ), which leads to deep eclipses ( $\Delta B \simeq 2.5 mag$ ) in the light curve every 1.5 hours when the white dwarf, accretion disk and bright spot are occulted by the mass-donor star. This allows the emission from the different light sources to be distinguished and spatially resolved studies to be performed, making V2051 Oph an excellent laboratory for the study of accretion physics. In particular, it is well suited for the application of indirect imaging techniques to resolve the disk emission both in position (eclipse mapping, Horne 1985) and velocity (Doppler tomography, Marsh

---

Departamento de Física, Universidade Federal de Santa Catarina, Trindade, 88040-900, Florianópolis, SC, Brazil

& Horne 1988).

V2051 Oph displays large amplitude flickering activity (up to 30 per cent of the total light in the optical), which is responsible for a variety of eclipse morphologies (e.g., Warner & Cropper 1983) and usually hampers the measurement of white dwarf and bright spot eclipse phases. Baptista et al. (1998) caught the star in an unusual faint brightness state ( $B \simeq 16.2$  mag) in which the mass accretion rate and flickering activity were significantly reduced, allowing a clean view of the white dwarf at disk center. They derived a mass ratio of  $q = 0.19 \pm 0.03$  and an inclination of  $i = 83.^\circ 3 \pm 1.^\circ 4$ .

Vrielmann et al. (2002) applied eclipse mapping techniques to multicolor data of V2051 Oph to find that the disk is brighter in the front side (the hemisphere nearer to the secondary) and interpreted this behavior as caused by enhanced emission from the bright spot. They also estimated a distance of  $d = 146 \pm 20$  pc for the system.

Kiyota & Kato (1998) observed V2051 Oph in superoutburst and detected superhumps in the light curve of the object, confirming its classification as an SU UMa star – a sub-class of dwarf novae with occasional superoutbursts  $\sim 0.7$  mag brighter and  $\sim 5$  times longer than an ordinary outburst. However, due to the complex behavior observed in V2051 Oph, Warner (1996) suggested a possible alternative classification of it as a polaroid, an intermediate polar with a synchronized primary.

Here we report the results of an optical and UV spectral mapping experiment of V2051 Oph in its faint brightness state of 1996 (e.g. Baptista et al. 1998). The details of the data analysis are given in Section 2. In Section 3 we investigate the disk spatial structure in the lines and continuum, and we present spatially resolved spectra of the disk, gas stream and uneclipsed light. The results are discussed in Section 4 and summarized in Section 5.

## 2. Data analysis

### 2.1. Observations

The Faint Object Spectrograph (FOS) onboard the Hubble Space Telescope (HST) was used to secure high-speed spectroscopy covering two con-

secutive eclipses of V2051 Oph on 1996 January 29 while the star was in an unusual low brightness state ( $B \simeq 16.2$  mag). The observations are summarized in Table 1. The first run covers a short phase range around the egress of an eclipse in the optical (G400H grating), and the second run covers the next eclipse in the UV (G160L grating). The reader is referred to Baptista et al. (1998) for a detailed description of the observations and data reduction procedures.

The average out-of-eclipse UV spectrum is shown in Fig. 1 (top). It displays emission lines of Ly $\alpha$   $\lambda 1216$  (mostly geo coronal), NV  $\lambda 1240, 1243$ , Si II  $\lambda 1300$ , C II  $\lambda 1336$ , Si IV  $\lambda 1394, 1403$ , C IV  $\lambda 1549, 1551$ , Si III  $\lambda 1892$ , C III  $\lambda 2297$ , as well as broad absorption bands reminiscent of those seen in OY Car (Horne et al. 1994), which were interpreted as a blend of Fe II lines. There is no evidence of He II  $\lambda 1640$  emission. The position of the second-order Ly $\alpha$  emission is illustrated in Figure 1 (top). The bottom panel of Figure 1 shows the average out-of-eclipse optical spectrum. It displays the Balmer continuum in emission, as well as He I, He II and strong Balmer emission lines. The optical emission lines show a clear double-peaked profile. The blue peak of the lines is stronger than the red peak because part of the disk side contributing redshifted line emission is still occulted by the secondary star at the phase range used to compute the average spectrum.

### 2.2. Light-curve construction

The UV spectra were divided into a set of 34 narrow passbands, with 22 continuum passbands 19–60 Å wide and 12 passbands for 10 lines (Fig. 1). The blue end of the spectra (shortward of the Ly $\alpha$  line) was not included in this analysis because of the very low count rate [and, consequently, low signal-to-noise ratio (S/N)] of the data in this spectral region. The emission lines were sampled in a single velocity bin 5000 or 6000 km s<sup>−1</sup> wide (centered at the rest wavelength,  $v = 0$  km s<sup>−1</sup>), except for the C IV line, which was separated in a bin centered at the rest wavelength and velocity-resolved bins for the blue and red wings of the line (all bins with  $\Delta v = 5000$  km s<sup>−1</sup>)<sup>1</sup>. The opti-

<sup>1</sup>The choice of the number (or width) of the passbands was constrained by the signal-to-noise (S/N) ratio of the resulting light curves. Narrower passbands lead to light curves

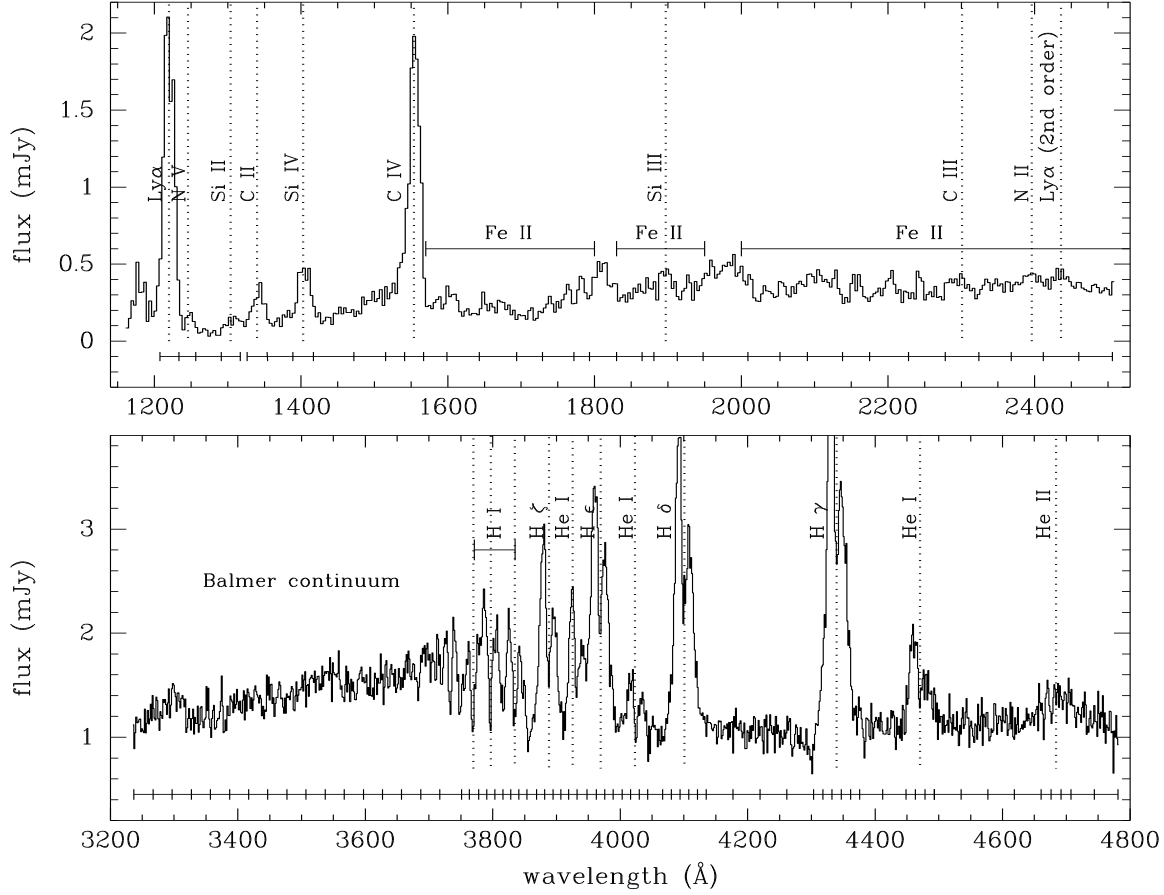


Fig. 1.— Average out-of-eclipse UV (G160L; top ) and optical (G400H; bottom) HST spectra of V2051 Oph. The phase ranges are  $+0.10$  to  $+0.20$  and  $+0.075$  to  $+0.080$  cycles, respectively, for the UV and optical spectra. The observations correspond to the eclipse cycles 109,988 (optical) and 109,989 (UV) according to the linear ephemeris of Baptista et al. (2003). Emission (vertical dotted lines) and absorption (horizontal lines) features are labeled. Horizontal tick marks indicate the passbands used to extract light curves (34 in the UV and 68 in the optical).

Table 1: Journal of the Observations.

Run	Start (UT)	Eclipse Cycle	Number of Exposures	Spectral Range Å	Phase Range (cycles)
H1	19:03	109,988	113	3226 – 4781	$+0.01, +0.08$
H2	20:24	109,989	693	1150 – 2507	$-0.09, +0.34$

cal spectra were divided into a set of 68 passbands, with 32 continuum passbands 15-42 Å wide and 36 passbands for 11 lines. The emission lines were resolved in velocity bins  $1000 \text{ km s}^{-1}$  wide, with one bin centered at the rest wavelength. The systemic velocity of V2051 Oph ( $\gamma \simeq 40 \text{ km s}^{-1}$ ; Watts et al. 1986) is both rather uncertain and much smaller than the width of the passbands and was neglected. For those passbands including emission lines the light curve comprises the total flux at the corresponding bin, with no subtraction of a possible continuum contribution.

Light curves were extracted for each passband by computing the average flux on the corresponding wavelength range and phase-folding the results according to the linear ephemeris of Baptista et al. (2003),

$$T_{\text{mid}}(\text{BJDD}) = 2\,443\,245.97752 + 0.062\,427\,8634\,E, \quad (1)$$

where  $T_{\text{mid}}$  gives the inferior conjunction of the white dwarf.

Light curves at two selected continuum passbands and for the CIV and H $\gamma$  lines can be seen in Figs. 2 and 3, respectively. The incomplete eclipse phase coverage of the H1 run is clear (Fig. 3).

### 2.3. Eclipse mapping

Maximum-entropy eclipse mapping techniques (Horne 1985, Baptista & Steiner 1993) were used to solve for a map of the disk brightness distribution and for the flux of an additional uneclipsed component in each band. The reader is referred to Baptista (2001) for a recent review on the eclipse mapping method.

As our eclipse map we adopted a flat grid of  $51 \times 51$  pixels centered on the primary star with side  $2R_{L1}$ , where  $R_{L1}$  is the distance from the disk center to the inner Lagrangian point. The eclipse geometry is defined by the inclination  $i$  and the mass ratio  $q$ . The mass ratio  $q$  defines the shape and the relative size of the Roche lobes. The inclination  $i$  determines the shape and extension of the shadow of the secondary star as projected onto the orbital plane. In this paper we adopted the values derived by Baptista et al. (1998),  $q = 0.19$  and  $i = 83^\circ$ , which correspond to an eclipse phase

width of  $\Delta\phi = 0.0662$  cycle. This combination of parameters ensures that the white dwarf is at the center of the map.

For the reconstructions we adopted the default of limited azimuthal smearing of Rutten et al. (1992), which is better suited for recovering asymmetric structures than the original default of full azimuthal smearing (e.g. Baptista et al. 1996). We used a radial blur width  $\Delta r = 0.0157R_{L1}$  and an azimuthal blur width  $\Delta\theta = 30^\circ$ .

The statistical uncertainties in the eclipse maps were estimated with a Monte Carlo procedure (e.g., Rutten et al. 1992). For a given narrow band light curve, a set of 20 artificial light curves was generated in which the data points were independently and randomly varied according to a Gaussian distribution with standard deviation equal to the uncertainty at that point. The light curves were fitted with the eclipse-mapping code to produce a set of randomized eclipse maps. These were combined to produce an average map and a map of the residuals with respect to the average, which yields the statistical uncertainty at each pixel. The uncertainties obtained with this procedure were used to estimate the errors in the derived radial brightness distributions, as well as in the spatially resolved spectra.

The Appendix presents the results of eclipse mapping simulations addressing the reliability of disk surface brightness reconstructions from light curves of incomplete phase coverage, such as those of run H1.

Light curves and respective eclipse maps at selected passbands for the continuum and for the strongest emission lines are shown in Figs. 2 and 3, respectively. Contour curves in these Figures enclose the regions of the eclipse maps at the  $3\sigma$  and  $5\sigma$  levels of statistical significance.

## 3. Results

### 3.1. Disk structure

Maps of the disk surface brightness distributions, calculated by the maximum entropy eclipse mapping method, allow us to obtain spatially resolved information about the disk emission. In this section we discuss the structures in the eclipse maps of the strongest lines in the spectrum, as well as in selected continuum passbands.

---

too noisy to produce reliable eclipse maps.

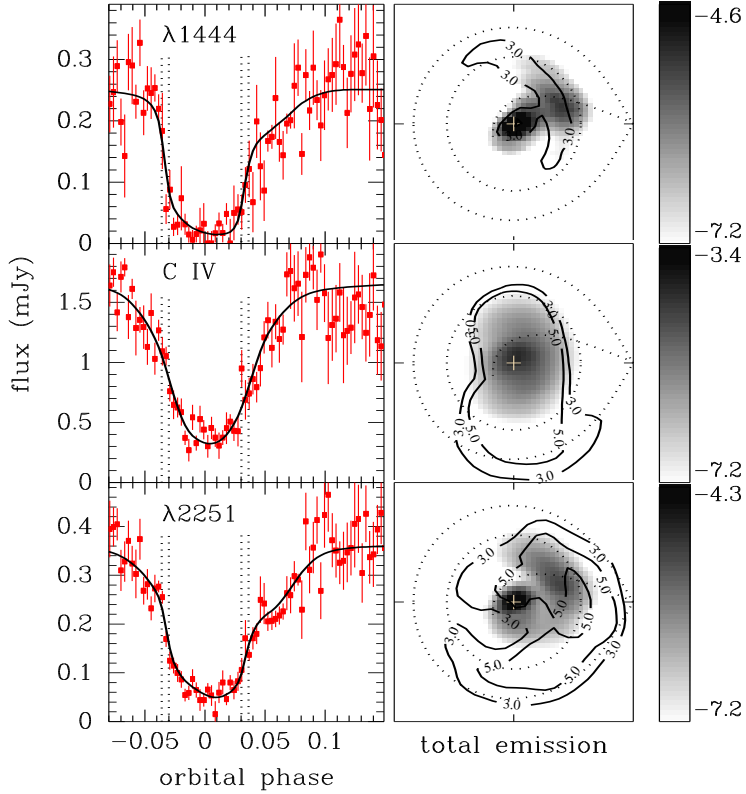


Fig. 2.— Data and model light curves and eclipse maps for the CIV line center ( $\Delta v = 5000 \text{ km s}^{-1}$ ) and for two selected continuum passbands in the UV. Left: Data (dots with error bars) and model (solid lines) light curves. Dotted lines mark the contact phases of the white dwarf eclipse. Right: Corresponding eclipse maps in a logarithmic gray scale. Brighter regions are shown in black, fainter regions in white. Contour curves enclose the eclipse map regions at the  $3\sigma$  and  $5\sigma$  levels of statistical significance. A cross marks the center of the disk; dotted lines show the Roche lobe, the gas stream trajectory, and a disk of radius  $0.56 R_{L1}$ ; the secondary is to the right of each map and the stars rotate counter-clockwise. The vertical bars indicate the logarithmic intensity level of the gray scale in each map.

Fig. 2 shows the light curves and respective eclipse maps for the CIV line center and for two selected UV continuum passbands. The S/N ratio of the light curves decreases towards the blue end of the spectrum. Accordingly, the statistical significance of the eclipse maps is lower in this spectral region. Thus, the brightest parts of the 1444 Å continuum map are only significant at the  $3\sigma$  level, while the eclipse maps in the red side of the spectrum are typically significant at the  $5\sigma$  confidence level.

The CIV line center light curve shows an inverse “Gaussian”-shaped eclipse with a minor asymmetry at egress and no sharp breaks in slope. Accordingly, the eclipse map shows a broad, smooth, and fairly symmetrical brightness distribution centered on the white dwarf, with no clear sign of the bright spot.

In contrast to what is observed in the CIV line center, the continuum light curves show sharp breaks in slope at the ingress and egress phases of the white dwarf plus a conspicuous asymmetric egress shoulder, indicating that there is significant additional emission from the disk side containing the bright spot. The corresponding eclipse maps display pronounced emission from the compact white dwarf at disk center plus an asymmetric structure in the disk side that is moving away from the secondary star (the upper hemisphere of the eclipse maps in Fig. 2) that can be associated with the gas stream emission.

The presence of bright compact structures in the continuum maps and their absence in the CIV line map, in addition to the observed spectrum of the uneclipsed component (see Section 4.4), are indications of the vertical extension and large optical depth of the gas from which the CIV line originates. Our interpretation is that the CIV line emission arises in a large gas region surrounding the disk. This region needs to be vertically extended and optically thick at this wavelength in order to veil the strong emission from the underlying white dwarf and bright spot. This is in line with expectations for an emission line produced by resonant scattering in a disk chromosphere. A similar result was found for the nova-like variable UX UMa (Baptista et al. 1995).

The eclipse map at 2251 Å is representative of most of the continuum maps. Aside from the asymmetry caused by the bright spot and gas

stream emission, it shows that another brightness asymmetry, namely, the disk hemisphere closest to the secondary star (the “front” disk side) is systematically brighter than the disk side farther away from the secondary star (hereafter called the “back” disk side). A similar effect was observed by Vrielmann et al. (2002), who interpreted it as a consequence of azimuthally-smeared bright spot emission. Our results will lead to a different interpretation (see Section 4.1).

Fig. 3 shows light curves and eclipse maps for the  $H\gamma$  line center ( $v = 0 \text{ km s}^{-1}$ ) and the blue ( $v = -1000 \text{ km s}^{-1}$ ) and red ( $v = +1000 \text{ km s}^{-1}$ ) line wing passbands. The velocity-resolved  $H\gamma$  line light curves show the expected behavior for the eclipse of gas rotating in the prograde sense (rotational disturbance), with the blue wing of the line reappearing from eclipse earlier than the red wing. The phase of maximum derivative in the three light curves coincides with the white dwarf egress phase, indicating that the maxima of the distributions are at the disk center. The light curves show deep eclipses with smooth and long lasting egresses. As a consequence, the resulting maps show fairly broad brightness distributions centered at the white dwarf position with an asymmetric bright source in the quadrant containing the bright spot. Simulations show that, in spite of the incomplete phase coverage of the optical light curves, it is possible to derive a fairly good reconstruction of the position and intensity of the white dwarf and bright spot in the corresponding eclipse maps (see the Appendix).

Fig. 3 (third and fourth columns) shows the net line emission and the net line absorption in each case. Net line emission/absorption maps are obtained by combining continuum eclipse maps on the short- and long-wavelength sides of the target emission line and by subtracting the derived average continuum map from each of the velocity-resolved line maps. Positive intensities in the resulting maps (third column, black and gray) signal the regions where the line appears in emission, while negative intensities (fourth column, black and gray) trace the regions where the line is in absorption. The net emission/absorption maps reveal that the Balmer lines are in emission over most of the accretion disk, but appear in absorption at the disk center and also in the region of the bright spot at the disk rim.

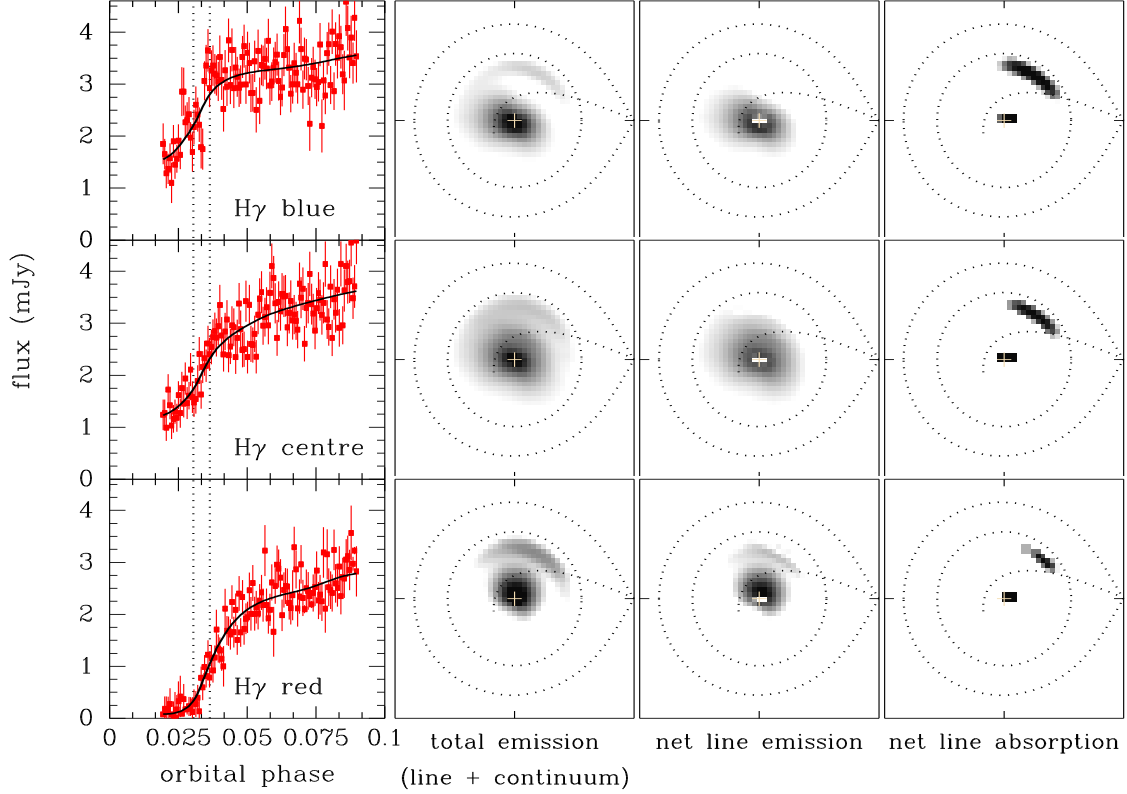


Fig. 3.— Left: Data (dots with error bars) and corresponding model (solid lines) light curves for the  $H\gamma$  line center passband ( $v = 0 \text{ km s}^{-1}$ ,  $\Delta v = 1000 \text{ km s}^{-1}$ ) and for its blue and red line wings ( $\Delta v = 1000 \text{ km s}^{-1}$ ). Second from left: Corresponding eclipse maps (total emission). Third from left: Eclipse maps of the net line emission. Right: Eclipse maps of the net line absorption in each case. The gray scale is the same in each column. The notation is similar to that of Fig. 2.

### 3.2. Spatially resolved spectra

Our set of monochromatic eclipse maps allows us to separate the spectra emitted by different parts of the accretion disk. Motivated by the distinct emission observed in the gas stream region and by the systematic difference in the emission from the opposite disk hemispheres, we sliced the disk into three distinct regions: “front”, “back” and “gas stream”. Azimuths are measured from the line joining both stars and increase counter-clockwise. We define “front” as the disk section between  $270^\circ$  and  $90^\circ$ , and “back” as the region between azimuths  $90^\circ$  and  $270^\circ$ . The region defined as “gas stream” is depicted in Fig. 4 (gray). In order to separate the disk spectra at different distances from the disk center, we further divided each of the disk regions in concentric annular sections of width  $\Delta R = 0.1 R_{L1}$ .

In order to minimize the possible contributions from the bright spot and gas stream to the disk “front” and “back” spectra we calculated the symmetric disk-emission component in each hemisphere. The symmetric component is obtained by slicing the disk into a set of radial bins and by fitting a smooth spline function to the resulting set of medians of the lower quartile of the intensities in each bin. The spline fitted intensity in each annular section is taken as the symmetric component. This procedure essentially preserves the baseline of the radial profile, removing all azimuthal structure. The statistical uncertainties affecting the fitted intensities are estimated with the Monte Carlo procedure described in Section 2.2.

The spatially resolved disk (front and back) spectra are shown in Fig. 5. The inner disk shows a flat continuum which becomes progressively fainter and redder with increasing radius, indicating the existence of a radial temperature gradient. The lines and the Balmer jump are in emission at all disk radii. The Balmer decrement becomes flatter and the lines are more prominent and narrower with increasing radii. The UV spectrum of the “front” side is perceptibly different from that of the “back” side. The comparison of the UV “front” and “back” spectra shows that the latter contains broad absorption bands, possibly due to FeII, that become more conspicuous in the outer parts of the disk – suggesting that it arises from absorption along the line of sight by a vertically

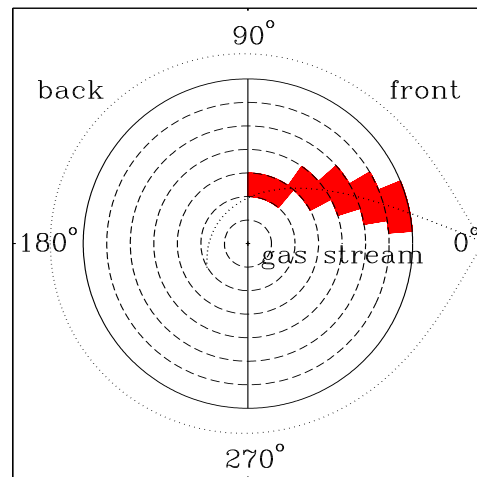


Fig. 4.— Schematic diagram showing the regions defined as “front”, “back” and “gas stream”. Dashed lines mark the annular regions of width  $0.1 R_{L1}$  used to extract spatially resolved spectra. Dotted lines show the projection of the primary Roche lobe onto the orbital plane and the gas stream trajectory. Azimuths are measured with respect to the line joining both stars and increase counter-clockwise. Four reference azimuths are labeled.



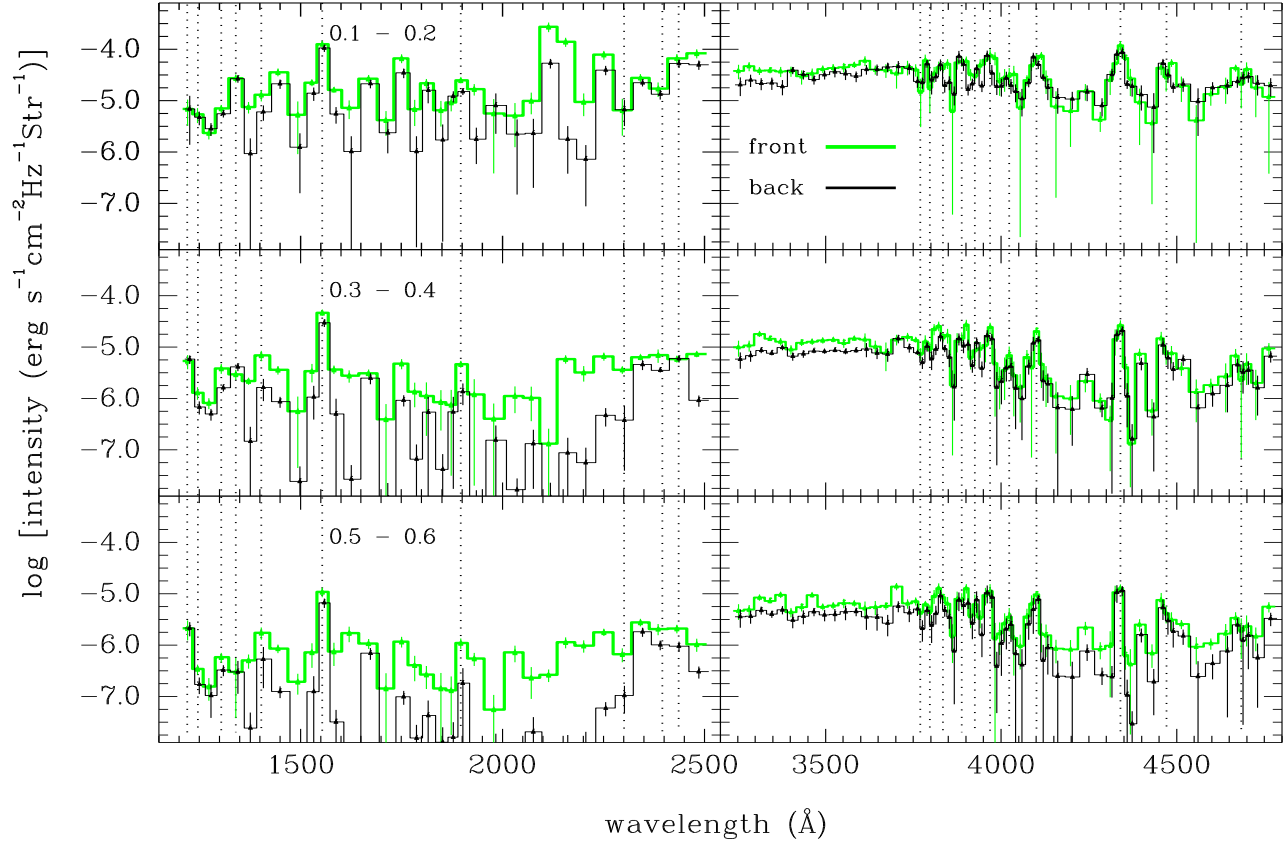


Fig. 5.— UV (left) and optical (right) spatially resolved disk spectra for the azimuthal sections defined as front ( $270^\circ - 90^\circ$ ) (gray) and back ( $90^\circ - 270^\circ$ ; black lines) for three selected annular regions (labeled in units of  $R_{L1}$ ). Vertical dotted lines mark the major transitions of the spectra.

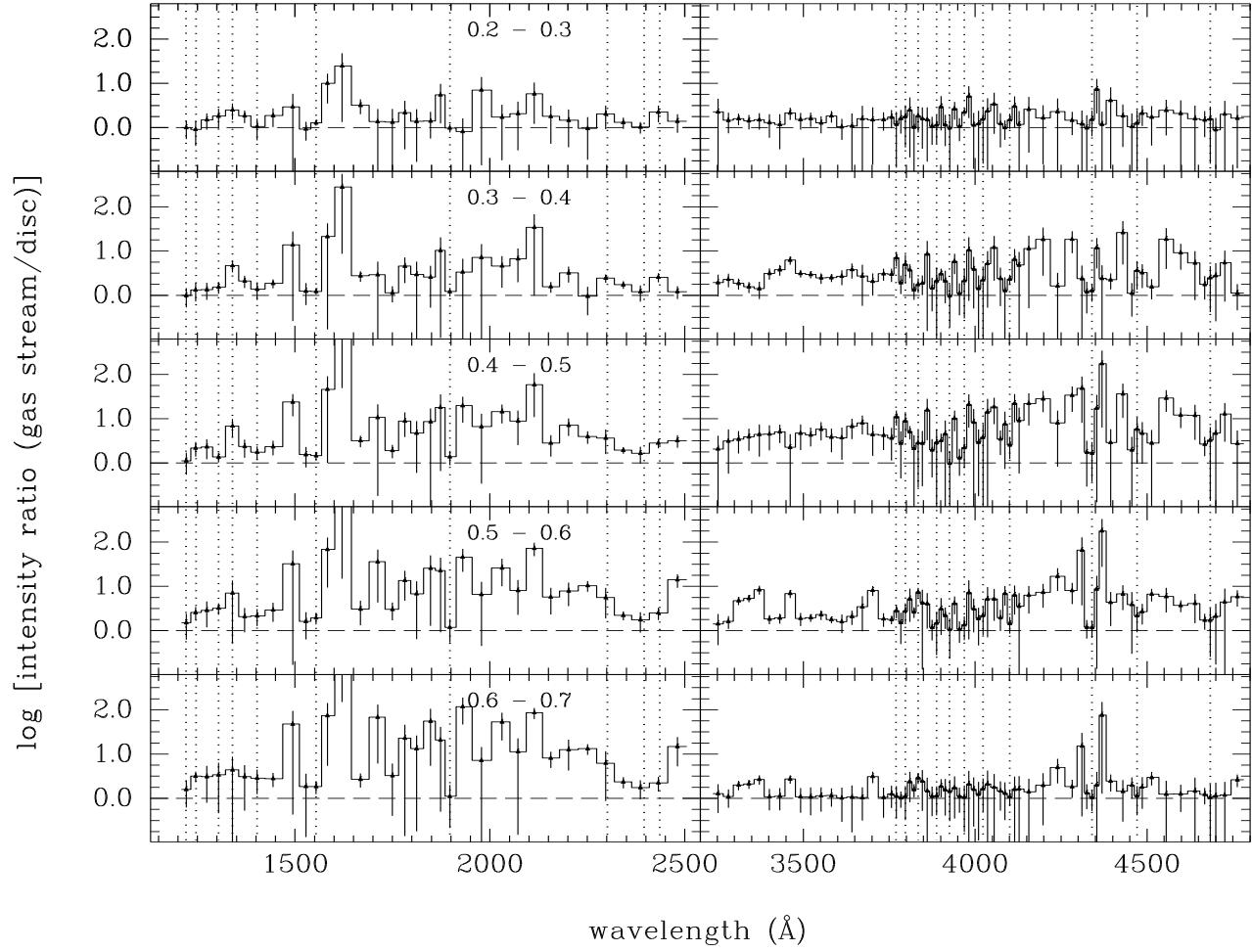


Fig. 6.— Ratio of the gas stream to the front disk spectra (see Fig. 4) as a function of radius. The notation is similar to that of Fig. 5.

extended region (e.g., Horne et al. 1994).

In order to investigate the emission along the gas stream trajectory, we calculate the ratio of the spectrum of the gas stream to the front disk symmetric component at the same radius (Fig. 6). The result reveals that the spectrum of the gas stream is typically 1 order of magnitude brighter than the disk spectrum in the intermediate and mainly in the outer disk regions ( $0.3 \lesssim R/R_{L1} \lesssim 0.7$ ) and this difference is significant at the  $3\sigma$  level. This result suggests the occurrence of gas stream overflow. This is in agreement with the results of Baptista & Bortoletto (2004), who found clear evidence of gas stream overflow in B band eclipse maps of V2051 Oph in quiescence.

In contrast to what is observed in the disk spectra, in which the lines appear in emission at all radii, in the ratio of the gas stream to the disk spectrum the CIV, Si III  $\lambda 1892$  and Balmer lines appear in absorption. This suggests the presence of matter outside of the orbital plane (e.g., chromosphere + wind) or that the disk has a non-negligible opening angle (flared disk). Horne et al. (1994) observed strong CIV emission out of the orbital plane in the dwarf nova OY Car in quiescence and suggested that this emission may arise from magnetic activity on the surface of the quiescent disk (Horne & Saar 1991) or from resonant scattering in a vertically-extended region well above the disk.

The slope of the continuum, the strength of the Balmer jump and the line intensities give a wealth of information about the physical conditions in the emitting gas. It is clear that simple blackbody and even stellar atmosphere models are not adequate to describe the strong line emission spectra of the V2051 Oph accretion disk. A more quantitative analysis of the spatially-resolved spectra demands optically thin disk models. This is beyond the scope of the present work and will be the subject of a forthcoming paper (A. Zobot et al. 2006, in preparation).

### 3.3. The emission lines

In this section we analyze the radial behavior of selected emission lines. Fig. 7 shows the radial intensity distributions for the lines and the adjacent continuum (top), the radial distributions of the net line emission (second from top), the ra-

dial run of the equivalent width (EW; third from top), and the radial run of the full width at half-maximum (FWHM; bottom) for the H $\delta$ , H $\gamma$ , He I 4471 and He II 4686 lines. The diagrams were computed for the disk “back” region to avoid contamination by gas stream emission and, as in Section 3.2, we used the symmetric disk-emission component in this analysis. We remind the reader that our line eclipse maps comprise the line emission plus any subjacent continuum contribution. The line distributions were obtained from the average of all eclipse maps along the line, while the continuum distributions were obtained from the average of the nearest continuum maps on both sides of each line. The net line emission distributions were computed by the subtraction of the adjacent continuum from the corresponding line distributions.

As expected, the intensity in the line maps is stronger than in the adjacent continuum (indicating that the lines appear in emission), except in the innermost disk regions, where the intensity of the continuum reaches that of the lines. For H $\delta$ , He I 4471 and He II 4686, the intensity in the line is equal or smaller than that of the adjacent continuum in the innermost annulus (indicating that the lines are in absorption in the white dwarf at the disk center) and were not plotted in the corresponding net line emission panels. The slope of the continuum distributions is steeper than that of the lines. The net line distributions decrease in strength with increasing disk radius. The lines are in emission at all disk radii with a radial dependency  $I \propto R^{-1.78 \pm 0.06}$ . This is steeper than the empirical  $I \propto R^{-1.5}$  law derived by Marsh et al. (1990) assuming a Keplerian distribution of velocities for the line emitting gas in the dwarf nova U Geminorum.

As a consequence of the radial behavior of the line and continuum intensity distributions, the lines are relatively weaker in the inner disk regions and their EW increases with increasing disk radius. H $\delta$  and H $\gamma$  are the dominant lines with an EW  $\simeq 300 \text{ \AA}$  at the disk edge ( $\simeq 0.5 R_{L1}$ ), while He I 4471 and He II 4686 have EW  $\simeq 100 \text{ \AA}$  at the same radius. In the innermost disk region ( $R < 0.1 R_{L1}$ ) the EW becomes negligible (or negative) because the continuum intensity reaches (or exceeds) the line intensities. Because of this, the FWHM in this region is also negligible and is not plotted in the corresponding FWHM panels.

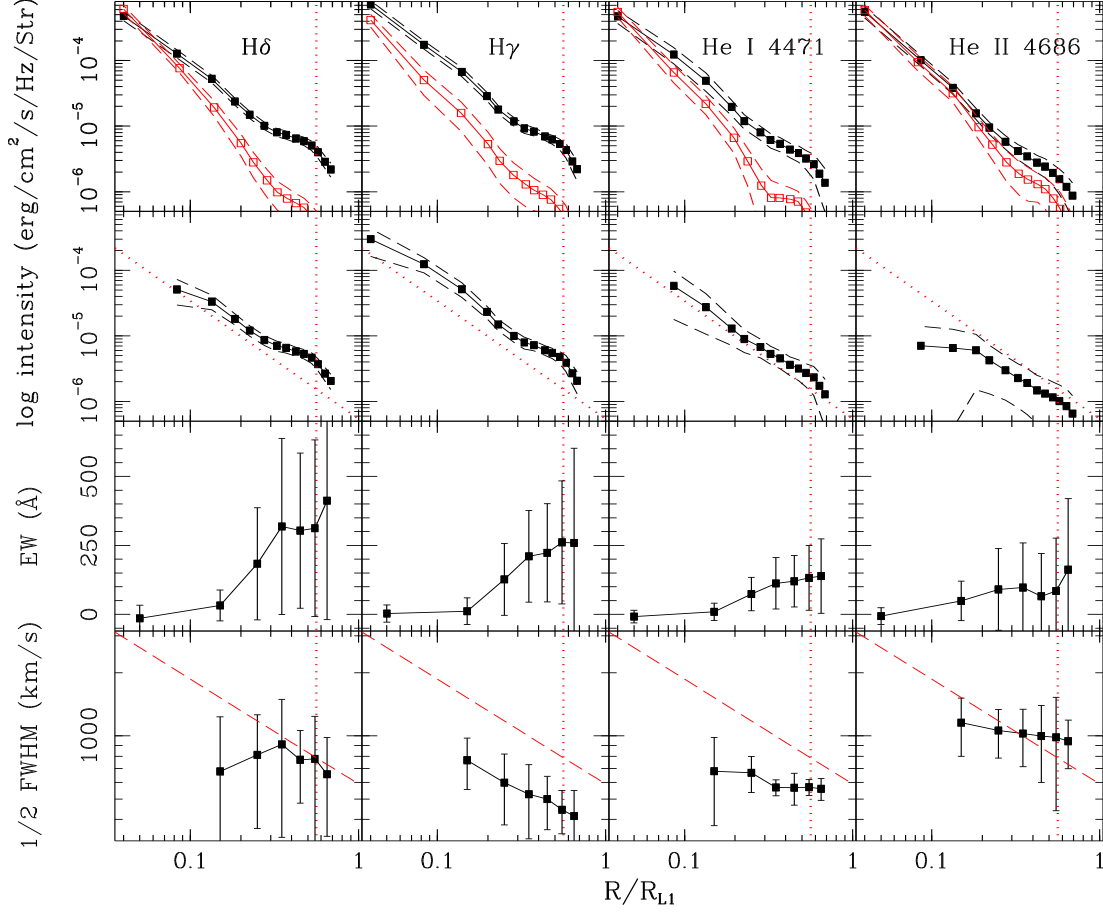


Fig. 7.— Top: Radial intensity distributions of selected optical lines (filled symbols) and of the corresponding adjacent continuum (open symbols). Dashed lines indicate the  $1\sigma$  limit in each case. Dotted lines mark the outer disk radius of  $R = 0.56R_{L1}$  (Baptista et al. 1998). Second from the top: Net line emission radial distributions. Dotted lines show the radial dependency for a slope  $I \propto R^{-1.78}$ . Third from top: EW as a function of radius. Bottom: FWHM of the lines as a function of radius. Dashed lines show the law  $v \propto R^{-1/2}$  expected for a gas rotating in Keplerian orbits.

H $\delta$  and He II 4686 show FWHM values comparable to those expected for a gas rotating in Keplerian orbits around an  $M_1 = 0.78 M_\odot$  white dwarf, but the slope of the radial distribution is flatter than the  $v \propto R^{-1/2}$  law. Because of the large uncertainties in the FWHM values, the distributions are still consistent with the Keplerian expectation. On the other hand, the H $\gamma$  and He I 4471 distributions are clearly different from the Keplerian expectation. Both lines show sub-Keplerian velocities (at the  $2-3\sigma$  confidence level). While the slope of the H $\gamma$  distribution is consistent with the  $v \propto R^{-1/2}$  law, He I 4471 shows a flat distribution, with velocities of  $1/2 \text{ FWHM} \simeq 600 - 700 \text{ km s}^{-1}$  at all radii.

### 3.4. The uneclipsed component

The uneclipsed component was introduced in the eclipse mapping method to account for the fraction of the total light that is not coming from the accretion disk plane (e.g. light from the secondary star or from a vertically-extended disk wind; Rutten et al. 1992).

Fig.8 shows the spectrum of the uneclipsed component, as well as its fractional contribution, as a function of wavelength. We estimated the fractional contribution of the uneclipsed component to the total flux by computing the ratio of the uneclipsed light to the average out of eclipse level at the corresponding passband.

The uneclipsed component is dominated by the Balmer continuum emission, strong Balmer and He emission lines in the optical, and resonant emission lines in the UV, suggesting that this light arises in a hot, vertically extended, optically thin gas region. Ly $\alpha$  is the strongest line in the uneclipsed spectrum ( $\simeq 30$  per cent of the total light at that wavelength). Nevertheless, most of this contribution is of geocoronal origin and not intrinsic to V2051 Oph. The remaining strong lines in the optical and UV spectra, as well as the Balmer continuum, account for  $\simeq 10$  per cent of the total light at the respective wavelength. The other continuum regions in the uneclipsed spectrum yield negligible fractional contributions to the total light. This indicates that the continuum emission comes mostly from the orbital plane while part ( $\simeq 10$  per cent) of the line emission arises in a vertically extended region above the disk.

## 4. Discussion

### 4.1. Evidences for chromospheric emission

Our continuum eclipse maps, particularly in the UV (Fig.2), show a front-back brightness asymmetry. This becomes clear when we compare the spectrum of the front and back disk sides (Fig.5): the front side of the disk is brighter than the back side. A similar result was found by Vrielmann et al. (2002). They discussed a few possibilities (non-negligible disk opening angle, warped disk, and bulge caused by impact of gas stream) but found no compelling explanation for the effect.

Our front and back disk spectra were computed from a symmetric disk component (see Section 3.2), which traces the baseline of the radial intensity distribution and removes the contribution of asymmetric brightness sources. Furthermore, the spectrum of the gas stream region is markedly different from the disk spectrum at intermediate and large radii ( $R \gtrsim 0.3 R_{L1}$ ). We are, therefore, confident that the observed front-back asymmetry is not an artifact caused by azimuthal smearing of bright spot emission, but it is a real effect.

Vrielmann et al. (2002) discussed the possibility that the observed asymmetry could be caused by a non-negligible opening angle ( $\alpha$ ) in the accretion disk, but they discarded this hypothesis because it would lead to an enhancement of the emission from the back side (seen at the lower effective inclination  $i_{eff} = i - \alpha$ ) in comparison to the front disk side (seen at a higher effective inclination  $i_{eff} = i + \alpha$ ). This argument is only correct if the disk atmosphere shows a stellar-type temperature decreasing with vertical height. If the disk has a chromosphere, in which the temperature actually increases with vertical height, the effect will be the opposite. Because the front disk side is seen at higher angles, the emerging photons will sample the uppermost (and hotter) chromospheric layers and the resulting spectrum will be brighter. The back disk side is seen through a lower inclination, allowing the emerging photons to come from deeper (and cooler) layers and leading to fainter intensities. Preliminary fits of the spatially resolved spectrum with LTE atmosphere models lead to effective temperatures for the front disk spectrum that are systematically higher than the temperatures of the back disk spectrum at the same radius (A. Zobot et al. 2006, in preparation),

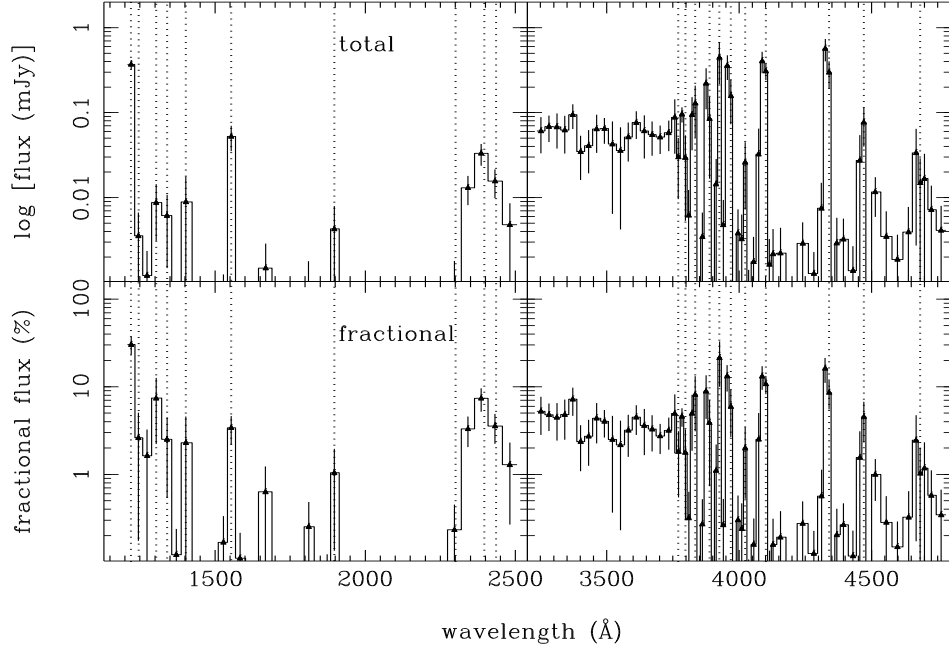


Fig. 8.— Spectrum of the uneclipsed component. Top: total contribution. Bottom: fractional contribution. The notation is similar to that of Fig. 5.

confirming the above scenario.

Therefore, the front-back asymmetry observed in the accretion disk of V2051 Oph can be interpreted as evidence of chromospheric emission from a disk with a non-negligible (but probably small) opening angle. This chromosphere is the site of the emission lines and is probably also responsible for the veiling of the continuum emission from the compact underlying white dwarf and bright spot. It may also account for the FeII absorption features that become more pronounced with increasing radius in the disk back side, because the photons arising from these regions travel an increasingly larger path across the vertically-extended disk chromosphere before leaving the binary and reaching the observer.

#### 4.2. The white dwarf spectrum and the distance

Here we fit white dwarf atmosphere models to the white dwarf spectrum in order to estimate the temperature of the primary star and the distance to the object. We adopted a white dwarf radius of  $R_{WD} = 0.0103 R_{\odot}$  and a Roche lobe size of

$R_{L1} = 0.422 R_{\odot}$  (Baptista et al. 1998). Therefore, our eclipse maps (see Section 2.3) have a scale factor of  $0.0392 R_{L1} \text{ pixel}^{-1}$ . Since the primary comprises a diameter of  $0.0488 R_{L1}$ , the central pixel of the eclipse map is fully contained in the white dwarf surface. We thus obtain a good estimate of the white dwarf spectrum by extracting the flux of the central pixel of the eclipse maps at each wavelength. These fluxes are multiplied by a factor

$$\frac{A_{WD}}{A_{pix}} = \left( \frac{0.0244 R_{L1}}{0.0392 R_{L1}} \right)^2 \frac{\pi}{\cos \theta}, \quad (2)$$

to scale the spectrum to the effective area of the white dwarf. The resulting spectrum shows a continuum filled with broad and shallow absorption lines plus a Balmer jump in absorption, resembling that of a DA white dwarf (Fig. 9).

We employed a grid of DA white dwarf spectra with  $6500 K < T_{WD} < 20000 K$  and  $\log g = 8$  (D. Koester 2000, private communication) in order to fit the V2051 Oph white dwarf spectrum. Since the DA white dwarf models only account for the continuum level and the HI lines, we masked the other line regions for the fitting procedure.

This includes removing the spectral region above 2300 Å in the UV spectrum and below 3400 Å in the optical spectrum, to avoid contamination by absorption bands due to Fe II. We considered two possibilities: (i) the inner disk is opaque and the visible part of the white dwarf surface is the projected area of the upper half hemisphere above the opaque disk, (ii) the white dwarf surface is fully visible through an optically thin disk.

Our best fit leads to a temperature of  $T_{WD} = 9500^{+2900}_{-1900}$  K for the white dwarf with a distance of  $d = 67^{+22}_{-25}$  pc if the inner disk region is opaque and  $d = 92^{+30}_{-35}$  pc if the inner disk is optically thin. Both the fitted temperature and the resulting distance are significantly different from previously reported values.

Catalán et al. (1998) made a preliminary fit to the G160L extracted white dwarf spectrum (assuming a white dwarf atmosphere model plus an intervening cool gas layer to account for the Fe II absorption bands) to find a white dwarf temperature of 15000 K. Their solution provides a reasonable fit in the UV but underestimates the white dwarf flux in the optical by a factor of 5. The white dwarf must be cooler (and, therefore, the distance must be smaller) to match the slope of the combined UV-optical spectrum. On the other hand, Vrielmann et al. (2002) fitted white dwarf atmosphere models to UBVRI photometric measurements to find  $T_{WD} = 19600$  K (if only the upper half of the white dwarf is visible) or  $T_{WD} = 15000$  K (if the white dwarf is fully visible) and  $d = 146$  pc. However, their result largely overestimates the white dwarf contribution in the UV. For comparison, Fig. 9 shows DA white dwarf models for the temperatures and respective distances obtained by the works mentioned above.

As a first step in trying to understand the difference, we investigate the possibility that some systematic error in the eclipse-mapping analysis (e.g. wavelength dependent blurring of bright central sources) is affecting the slope of the extracted white dwarf spectrum. To test this hypothesis, we extract the white dwarf spectrum by measuring the height of the jump in flux at white dwarf egress in the set of narrow band UV and optical light curves used for eclipse mapping. This provides an estimate of the white dwarf flux as seen during egress and is quite similar to the procedure used by Catalán et al. (1998) to extract the

UV white dwarf spectrum. The resulting spectrum is consistent with that of Fig. 9 under the uncertainties. We are therefore confident that the red slope of the white dwarf spectrum of V2051 Oph at the time of the HST observations is real. Thus, the main point is that, it is not possible to model the observed white dwarf spectrum with a hot ( $T_{WD} \gtrsim 14000$  K) DA atmosphere model.

The origin of the discrepancy between our result and the previous analyses may be in the restricted spectral coverage of the data used in those works. Catalán et al. (1998) used only the UV part of the spectrum (1150 – 2500 Å) to fit the white dwarf temperature. It is possible to match the observed UV intensities with a DA spectrum of 15000 K for a distance of  $d = 184$  pc (Vrielmann et al. 2002) at the expense of a large mismatch in the optical.

The slope of a DA white dwarf spectrum is very similar in the optical (3500 – 5000 Å) for a large range of temperatures. Therefore, the optical spectrum alone does not provide a strong constraint to the white dwarf temperature. We tested this by fitting white dwarf models only to the optical part of the spectrum. This exercise shows that it is possible to fit temperatures in the range 6500 – 16500 K with a  $\chi^2$  only 20% larger than the  $\chi^2$  of the best-fit model in this case,  $T_{WD} = 11500$  K. This lack of sensitivity affects the white dwarf temperature determination of Vrielmann et al. (2002), since they used only optical photometric data in their analysis. Moreover, they mistakenly took the value  $R_{WD} = 0.0244 R_{\odot}$  as the white dwarf radius, while the value quoted by Baptista et al. (1998) is  $R_{WD} = 0.0103 R_{\odot}$ . To compensate for the larger radius assumed for the white dwarf, their fit had to increase the distance by a similar amount (a factor of  $\sim 2.3$ ).

Steeghs et al. (2001) used optical spectroscopy (4000 – 6800 Å) to find that a (15000 K) blackbody was a good match to the slope of their extracted white dwarf spectrum. Their result faces the same problem discussed above; the slope of the optical continuum is very similar for a large range of temperatures.

It is important to notice that at the time of our observations V2051 Oph was in an unusual low brightness state, in which mass accretion may have been considerably reduced (Baptista et al. 1998). With reduced (or absent) accretional heat-

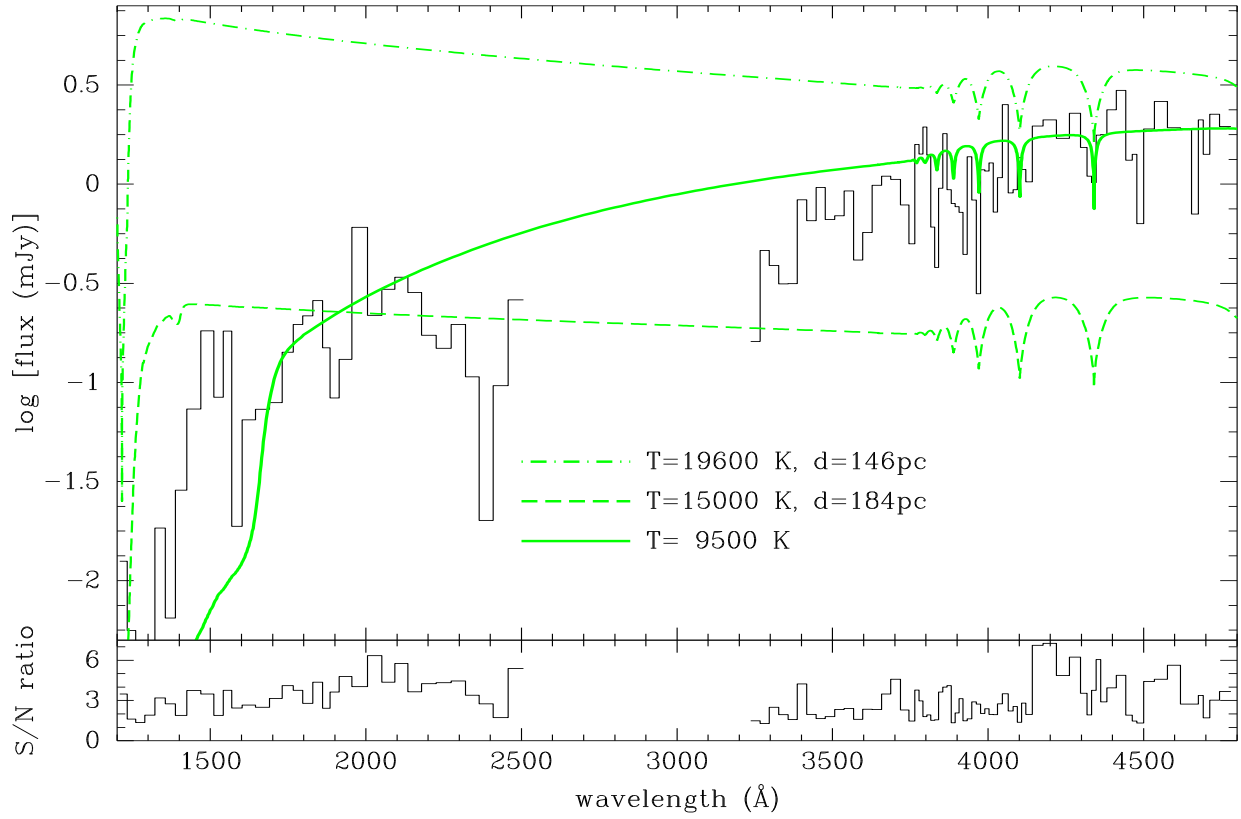


Fig. 9.— Spectrum of the V2051 Oph white dwarf (histogram) and DA white dwarf model fits. The dot-dashed line corresponds to a model with  $T = 19600\text{ K}, d = 146\text{ pc}$  (Vrielmann et al. 2002), and the dashed line correspond to a model with  $T = 15000\text{ K}, d = 184\text{ pc}$  (Catalán et al. 1998). The best fit model is displayed as a solid line. The bottom panel shows the S/N of the the white dwarf spectrum.



ing, it is possible for the white dwarf to cool down. We therefore expect that our fitted white dwarf temperature is lower than that during a normal, quiescent state.

Our larger spectral coverage, combining optical and UV data, allows a better determination of the slope of the white dwarf spectrum, and, therefore, its temperature and distance. Our results show that the distance to V2051 Oph is smaller than previously found.

## 5. Conclusions

The main results of our spectroscopic study of V2051 Oph in a faint brightness state during 1996 can be summarized as follows:

1. The presence of white dwarf and bright-spot strong emission in the continuum maps and their absence in the line maps, coupled with the significant extra absorption in the spectra of the back disk side, are indications of the vertical extension and large optical depth of the gas from which the lines originate.
2. Distinct emission along the stream trajectory suggests the occurrence of gas stream overflow.
3. Spatially resolved spectra show that the lines are in emission at all disk radii. The Balmer decrement becomes shallower with increasing radius.
4. The FWHM of the emission lines differs from that expected for a gas in Keplerian rotation and the line intensities drop with a radial dependency of  $I \propto R^{-1.78 \pm 0.06}$ .
5. The spectrum of the uneclipsed light is dominated by strong emission lines and a Balmer jump in emission, indicating origin in a hot, vertically extended, optically thin gas region above the disk. The strongest uneclipsed lines contribute  $\simeq 10$  per cent of the total flux.
6. Strong absorption bands, possibly due to Fe II, are seen in the spectra of the back disk side, suggesting it arises from absorption by an extended gas region above the disk.

7. The front disk spectrum is systematically brighter than the back disk spectrum at the same radius. This can be explained in terms of chromospheric emission (higher temperatures at the uppermost atmospheric layers) from an accretion disk with a non-negligible opening angle (limb brightening effect).
8. We fit stellar atmosphere models to the extracted white dwarf spectrum to find a temperature  $T_{WD} = 9500^{+2900}_{-1900} K$  and a distance of  $d = 67^{+22}_{-25} pc$  (if the inner disk is opaque) or  $d = 92^{+30}_{-35} pc$  (if the inner disk is optically thin).

*Acknowledgments.* We thank the anonymous referee for useful comments and suggestions. The white dwarf atmosphere models used in this work were kindly provided by Detlev Koester. This work was partially supported by CNPq/Brazil through the research grant 62.0053/01-1 – PADCT III/Milenio. RB acknowledges financial support from CNPq/Brazil through grants n. 300.354/96-7 and 301.442/2004-5. RKS acknowledges financial support from CAPES/Brazil and CNPq/Brazil.

### A. Reconstruction of maps from light curves with incomplete phase coverage

Here we address the reliability of eclipse-mapping brightness reconstructions for the case of light curves with incomplete phase coverage, such as those of run H1.

In order to simulate the structures observed in the optical maps, we created artificial eclipse maps of  $51 \times 51$  pixels with two compact Gaussian spots, one at the disk center (the white dwarf) and another near the impact region of the gas stream with the disk (the bright spot), on top of a low-intensity, broad Gaussian background to simulate a faint accretion disk. The artificial map is shown in Fig. 10.

We simulated the eclipse of the artificial map using the geometry of V2051 Oph ( $i = 83^\circ$  and  $q = 0.19$ , Baptista et al. 1998) to create light curves with added Gaussian noise reproducing the S/N of the V2051 Oph data ( $S/N = 10$ ). Since the optical light curves of V2051 Oph have incomplete phase coverage, we truncated the synthetic light curves to reproduce the set of orbital phases of the optical run. Fig. 10 shows light curves for a complete phase coverage and for the set of phases of the V2051 Oph optical data. We applied eclipse mapping techniques to the two light curves and compared the results with the original map.

The ability of the eclipse-mapping method to construct a two-dimensional surface brightness map from a one-dimensional eclipse light curve stems from the fact that ingress and egress arches intersect with each other at relatively large angles (Horne 1983). Fig. 11 illustrates the eclipse geometry of V2051 Oph for the incomplete set of phases of run H1. Arches drawn on the eclipse map connect points of constant ingress and egress phases. The pair of thick lines shows the ingress/egress arches for the first phase of the light curve ( $\phi = +0.0194$ ). Each pair of arches outlines a region of the disk that is being occulted by the shadow of the secondary star at a given phase (for visualization purposes, Fig. 11 shows only one of every three phases/arches in the incomplete light curve).

The effect of incomplete phase coverage is to reduce the information available to reproduce structures in parts of the accretion disk. For the light curve with incomplete phases, about 40 % of the disk surface is not covered by ingress or egress arches (Fig. 11). There is no information in the eclipse shape about the brightness distribution of the disk regions not sampled by the grid of arches. Therefore, the disk side approaching the secondary star (the lower hemisphere of the map in Fig. 10) will not affect the shape of the eclipse light curve with the incomplete set of phases and its brightness distribution will not be recovered by the eclipse-mapping method.

Fig. 10 shows that the structures are reasonably well reconstructed with the light curve of full eclipse phase coverage. As a consequence of the intrinsic azimuthal smearing effect of the eclipse mapping technique (see Baptista 2001 for more details) the asymmetric spot appears smeared into a crescent-shaped structure. Because the light curve with incomplete phase coverage lacks most of the ingress phases, the technique is not able to properly reconstruct structures located in the disk region that approaches the secondary. However, for this V2051 Oph simulation the main brightness structures are in the disk center and in the bright spot region (the disk hemisphere moving away from the secondary star), and the reconstruction is reasonably good and quite similar to that obtained with the complete eclipse phase coverage. The radial intensity distributions of the eclipse maps from the complete and incomplete phase coverage light curves (not shown) are very similar, with only small differences that are within the uncertainties of the distributions.

In summary, the simulations show that, although the eclipse mapping method is not able to recover structures in disk regions for which there is no information in the eclipse shape, brightness distributions with structures in the disk center and in the bright spot region can still be detected in eclipse maps derived from light curves with an incomplete phase coverage such as that of run H1, in spite of their relatively low S/N.

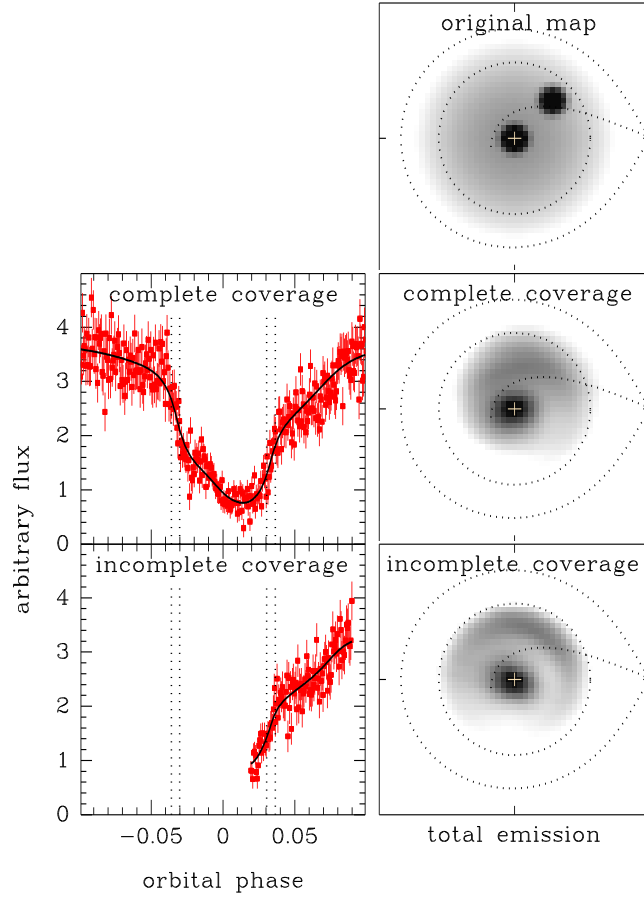


Fig. 10.— Left: Synthetic light curves with  $S/N=10$  for the full phase coverage (top) and for the phase set of the optical run (bottom). Right: Original map and reconstructions obtained from the light curves in the left panels. The notation is the same as in Fig. 2.

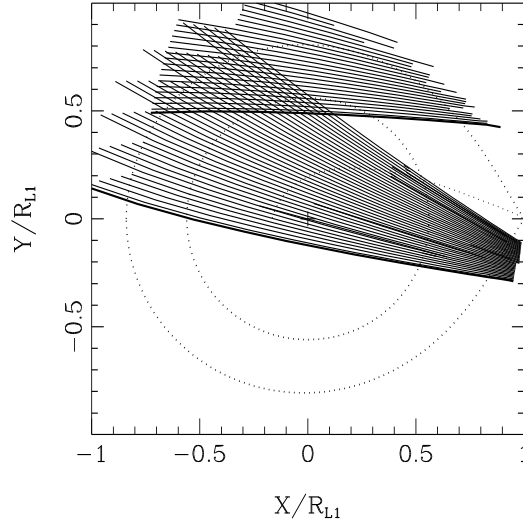


Fig. 11.— Eclipse geometry of V2051 Oph for the set of phases of the optical run. Arches (solid lines) connect points of constant ingress and egress phases. To avoid overcrowding the figure, only one phase/arch of every three is shown. The pair of thick lines shows the ingress and egress arches for the first phase of the light curve ( $\phi = +0.0194$ ). Dotted lines depict the primary Roche lobe, a disk of radius  $0.56 R_{L1}$  and the ballistic stream trajectory.

## REFERENCES

- Baptista, R. 2001, LNP Vol. 573: Astrotomography, Indirect Imaging Methods in Observational Astronomy, 573, 307
- Baptista, R., Borges, B. W., Bond, H. E., Jablonski, F., Steiner, J. E., & Grauer, A. D. 2003, MNRAS, 345, 889
- Baptista, R., & Bortoletto, A. 2004, AJ, 128, 411
- Baptista, R., Catalán, M. S., Horne, K., & Zilli, D. 1998, MNRAS, 300, 233
- Baptista R., Harlaftis E. T., & Steeghs D. 2000. MNRAS, 314, 727
- Baptista, R., Horne, K., Hilditch, R. W., Mason, K. O., & Drew, J. E. 1995, ApJ, 448, 395
- Baptista R., & Steiner J. E. 1993. A&A, 277, 331
- Baptista R., Steiner J. E., & Horne K. 1996, MNRAS, 282, 99
- Bateson, F.M. ed., 1980, Var. Star. Circs. R. Astron. Soc., New Zealand
- Catalán, M. S., Horne, K., Cheng F. H., Marsh T. R., & Hubeny I. 1998, ASP Conf. Ser. 137: Wild Stars in the Old West, 137, 426
- Cook, M. C., & Brunt, C. C. 1983, MNRAS, 205, 465
- Horne, K. 1983, Ph.D. Thesis, Caltech
- Horne K. 1985. MNRAS, 213, 129
- Horne, K., Marsh, T. R., Cheng, F. H., Hubeny, I., & Lanz, T. 1994, ApJ, 426, 294
- Horne, K., & Saar, S. H. 1991, ApJ, 374, L55
- Hubeny, I. 1998. Comp. Phys. Comm. 52, 103
- Kiyota, S., & Kato, T. 1998, Information Bulletin on Variable Stars, 4644, 1
- Marsh T. R., & Horne K. 1988. MNRAS, 235, 269
- Marsh, T. R., Horne, K., Schlegel, E. M., Honeycutt, R. K., & Kaitchuck, R. H. 1990, ApJ, 364, 637
- Rutten R. G. M., van Paradijs J., & Tinbergen J. 1992, A&A, 254, 159
- Sanduleak, N. 1972, Information Bulletin on Variable Stars, 663, 1
- Steeghs, D., O’Brien, K., Horne, K., Gomer, R., & Oke, J. B. 2001, MNRAS, 323, 484
- Vrielmann, S., Stiening, R. F., & Offutt, W. 2002, MNRAS, 334, 608
- Warner, B. 1996, Ap&SS, 241, 263
- Warner, B., & Cropper, M. 1983, MNRAS, 203, 909
- Warner, B., & O’Donoghue, D. 1987, MNRAS, 224, 733
- Watts, D. J., Bailey, J., Hill, P. W., Greenhill, J. G., McCowage, C., & Carty, T. 1986, A&A, 154, 197